JOURNAL OF OPTOELECTRONICS AND ADVANCED MATERIALS Vol. 10, No. 4, April 2008, p. 732 - 736

Invited Paper

Nanoscale metallic and composite biomaterials

M. JURCZYK[*,a], K. NIESPODZIANA[a] , M. TULINSKI[a], K. JURCZYK[b]
[a]*Institute of Materials Science and Engineering, Poznan University of Technology, M. Skłodowska-Curie 5 Sq., 60-965 Poznan, Poland*
[b]*K. Marcinkowski University of Medical Sciences, Department of Conservative Dentistry and Periodontology, Bukowska 70, 60-812 Poznan, Poland*

The paper reviews research at Poznan University of Technology, on the synthesis of nanoscale metallic and composite biomaterials. These materials were prepared by the combination of mechanical alloying and powder metallurgical process. Examples of the materials include nanocrystalline nickel-free stainless steels and titanium-ceramic nanocomposites, both for biomedical applications. The results show an enhancement of properties due to the nanoscale structures in bulk consolidated materials. The mechanical and corrosion properties of produced biomaterials are presented. For example, microhardness test showed that nanocrystalline austenitic nickel-free nitrogen containing stainless steel and Ti-10vol% hydroxyapatite samples exhibits Vickers microhardness as high as 378 $HV_{0.2}$ and 1500 $HV_{0.2}$, respectively. The hardness is almost two and five times greater than in austenitic steel obtained by conventional method or microcrystalline titanium, respectively. From the point of view of mechanical and corrosion properties, Ti-10 vol% HA or SiO_2 nanocomposite are promising biomaterials for use as hard tissue replacement implants.

(Received February 25, 2008; accepted April 2, 2008)

Keywords: Bionanomaterials, Mechanical alloying, Ni-free stainless steel, Ti-HA (SiO_2) nanocomposites

1. Introduction

Mechanical alloying (MA) technique has been proved a novel and promising method for alloy formation. MA was developed in the 1970's at the International Nickel Co as a technique for dispersing nanosized inclusions into nickel-based alloys [1]. During the last years, the MA process has been successfully used to prepare a variety of alloy powders including powders exhibiting supersaturated solid solutions, quasicrystals, amorphous phases and nano-intermetallic compounds [1, 2]. The mechanism of amorphous phase formation by MA is due to a chemical solid state reaction, which is believed to be caused by the formation of a multilayer structure during milling [2].

The raw materials used for MA are commercially available as high purity powders that have sizes in the range of 1-100 μm. During the mechanical alloying process, the powder particles are periodically trapped between colliding balls and are plastically deformed. Such a feature occurs by the generation of a wide number of dislocations as well as other lattice defects. Furthermore, the ball collisions cause fracturing and cold welding of the elementary particles, forming clean interfaces at the atomic scale. Further milling leads to an increase of the interface number and the sizes of the elementary component area decrease from millimeter to submicrometer lengths. Concurrently to this decrease of the elementary distribution, some nanocrystalline intermediate phases are produced inside the particles or at its surfaces. As the milling duration develops, the content fraction of such intermediate compounds increases leading to a final product which properties are the function of the milling conditions. The milled powder is finally heat treated to obtain the desired microstructure and properties. Annealing leads to grain growth and release of microstrain.

Over the past years, nanoscale materials, also called nanomaterials have attracted enormous amounts of interest from researchers. Nanomaterials can be metals, ceramics, polymers and composite materials which demonstrate novel properties compared to conventional (polycrystalline) materials due to their nanoscale features [3]. Examples of the materials include nanocrystalline nickel-free stainless steels and titanium-ceramic nanocomposites. Till now, it has been shown, that implants made from metallic bionanomaterials improved considerably the prosthesis ultimate strange and their biocompatibility [4-7].

Presently, most biomedical implants, e.g. stents, consist of a stainless steel framework. The main disadvantage of the most popular austenitic stainless steel (316L) is lack of biocompatibility, toxicity of corrosion products and fracture due to corrosion fatigue [8]. Austenite stabilizer - nickel - is reported to be an especially toxic element which causes allergies and even cancer. One of the most promising austenitizing elements to replace nickel is nitrogen.

Recently, a new manufacturing process of nickel-free austenitic stainless steels with nitrogen absorption treatment has been developed [7]. In this method, small devices can be precisely machined in a ferritic phase and than during nitrogenization of their surfaces in nitrogen gas at temperature approx. 1200 ^{o}C they become nickel-free austenitic stainles steels with better mechanical and corrosion resistance properties.

On the other hand, Ti and its alloys possess favorable properties, such as relatively low modulus, low density, high strength. Apart from that, these alloys are generally regarded to have good biocompatibility and high corrosion resistance, but cannot directly bond to the bone [9]. In addition, metal implants may loose and even separate from surrounding tissues during implantation [10-12]. Titanium and titanium based alloys have relatively poor tribological

properties because of their low hardness [9]. One of the methods that allow the change of biological properties of Ti alloys is to produce a composite, which will exhibit the favorable mechanical properties of titanium and excellent biocompatibility and bioactivity of ceramic. The most commonly ceramics, used in medicine are hydroxyapatite, silica or bioglass. The ceramic coating on the titanium, improves the surface bioactivity, but often flakes off as a result of poor ceramic/metal interface bonding. So, composite materials containing titanium and ceramic as a reinforced phase are expected to have broad practical applications.

The paper reviews research at Poznan University of Technology, on the synthesis of nanoscale metallic and composite biomaterials. Examples of the materials include a nanocrystalline nickel-free stainless steels and a titanium-ceramic nanocomposites. The aim of the present work was to study the structure, mechanical and corrosion properties of nickel-free austenitic stainless steels with nanostructure, Ti-HA (3, 10 vol%) and Ti-SiO_2 (3, 10 vol%) nanocomposites, prepared by mechanical alloying and powder metallurgical process.

2. Experimental details

The FeCrMnMoN alloys and titanium-ceramic nanocomposite materials with different content of hydroxyapatite or silica were prepared by mechanical alloying of stoichiometric amounts of the constituent elements (99.9% or better purity). Mechanical alloying was carried out using a SPEX 8000 Mixer Mill fitted with a hardened steel vial and 10 mm diameter steel balls. The as-milled FeCrMnMo powders were heat treated at 750^{o}C for 0.5 h, under high purity argon, to form ordered phases. Nitrogenation of cold pressed samples was carried out at temperature 1215 ^{o}C for 24 hours at 120 kPa nitrogen pressure.

The titanium-ceramic nanocomposite materials with different content of hydroxyapatite or silica were prepared by mechanical alloying and powder metallurgical process. The mixture of Ti-HA (3, 10 vol%) and Ti-SiO_2 (3, 10 vol%) powders were first ball milled for 44 and 20 hours, respectively and then compacted at 20 MPa. Finally green compacts were heat treated at 1150 ºC for 2 h under a gas atmosphere composed of 95% Ar and 5% H_2 to form ordered phases.

The powders were characterized by means of X-ray diffraction (XRD) and scanning electron microscopy (SEM) with an energy-dispersive X-ray microanalysis system (EDS). XRD was performed using an X-ray powder diffractometer with Co Kα radiation, at various stages during milling, prior to annealing and after annealing as well as after nitrogenation. The TEM images and selected area electron diffraction (SAED) patterns were recorded with a Philips CM 20 Super Twin microscope, which provides a 0.24 nm resolution at acceleration voltage of 200 kV.

Microhardness measurements were carried out in Vickers method with the load of 200g. The micrographs were obtained using an optical microscope. The density of the sintered samples was determined by the Archimedes method.

The analyses of the corrosion were conducted on a Solartron 1285 potentiostat in Princeton Applied Research corrosion cell system. The corrosion resistance in 1M H_2SO_4 distilled water solution was measured using in vitro potentiodynamic corrosion test. The counter electrode consisted of two graphite rods and saturate calomel solution and was used as the reference electrode. The surface area exposed to the electrolyte was 0.8 mm^2. The polarization curves were obtained for each specimen. Corrosion potentials (E_C) and corrosion current densities (I_C) were determined by Tafel extrapolation methods. The corrosion rate, C_R (rate of metal dissolution), in millimeters per year, was estimated with the following equation:

$$CR = \frac{I_C \cdot EW}{F \cdot \rho} \tag{1}$$

where I_C is a corrosion current density (μA/cm^2), EW is an equivalent weight of the corroding species in grams (g), ρ is the density of the corroding species (g/cm^3) and F is the Faraday constant (96,500 As/mol).

3. Results and discussion

In the present work, nanocrystalline nickel-free austenitic stainless steels and Ti-ceramic nanocomposites have been prepared by mechanical alloying (see Tables 1 and 2).

3.1. Nickel-free austenitic stainless steels

The X-Ray diffraction patterns on Fig. 1 are representative of a $Fe_{74}Cr_{24}Mo_2$ alloy after MA, annealing and nitrogenation under different conditions. First diffraction pattern shows a mixture of initial powders (Fig. 1a). After 48 h of MA the alloy had decomposed into an amorphous phase and nanocrystalline α-Fe (Fig. 1b). Heat treatment performed after MA process results in crystallization into ferritic phase (Fig. 1c). Then, compacted material was nitrided at 1215 ^{o}C which results in phase transformation from ferritic to fully austenitic (Fig. 1d). Crystallite size of so produced material, 27 nm, was estimated by Scherrer's method.

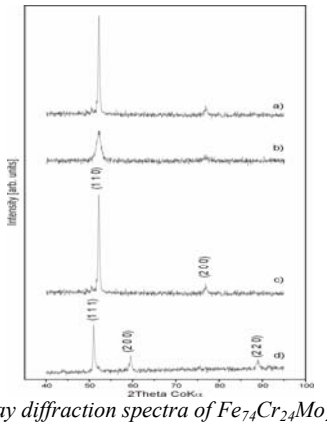

Fig. 1. X-ray diffraction spectra of $Fe_{74}Cr_{24}Mo_2$ material: a) mixture of initial powders, b) after 48 hours of mechanical alloying, c) after heat treatment 750 ^{o}C/0.5h, d) after nitrogen absorption.

EDX analysis (Fig. 2) of $Fe_{74}Cr_{24}Mo_2$ alloy confirms that in the material's matrix there is 74% of iron, 20% of chromium and 3% of molybdenium. Content of nitrogen in this case is 0.56% and 2.47% content of oxygen. Oxygen content in syntesized materials was carried out using XPS method. At the grain boundaries one can observe small content of manganese and increase of oxygen content to 7% at. Dependent on region, nitrogen content is changing from 0 to 2.16% due to diffusion effects.

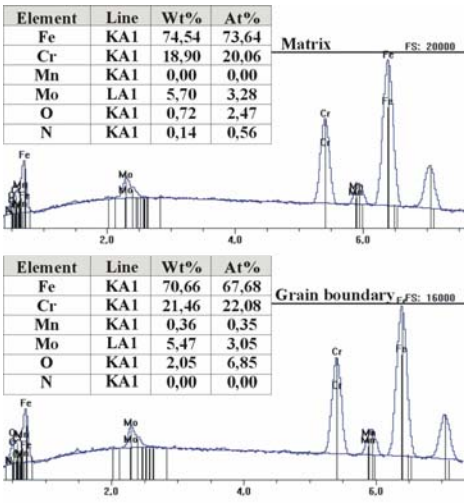

Fig. 2. EDX analysis in matrix and at the grain boundary of $Fe_{74}Cr_{24}Mo_2$ sample.

The microhardness of the final bulk material was studied using Vickers method and the results are presented on Fig. 3. Compared with A240 commercial austenitic stainless steel (195 $HV_{0.2}$), pure titanium (266 $HV_{0.2}$), TiNi alloy (279 $HV_{0.2}$) and widely used in medicine 316L stainless steel (248 $HV_{0.2}$), microhardness of sintered nanocrystalline austenitic nickel-free nitrogen containing stainless steels obtained by mechanical alloying is significantly higher (378 to 487 $HV_{0.2}$). The result is almost two times greater than in austenitic steel obtained by conventional methods. This effect is directly connected with structure refinement and obtaining of nanostructure.

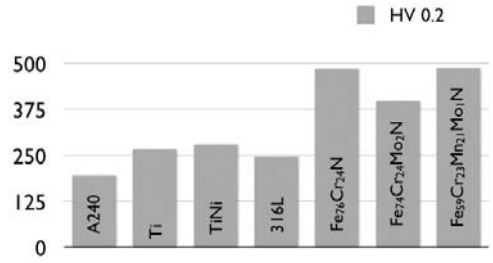

Fig. 3. Microhardness of produced FeCrMoN materials compared to A240 and 316L stainless steels, pure titanium and microcrystalline TiNi alloy.

The general shape of the potentiodynamic curves is shown on Fig. 4. Results of corrosion test are listed in Table 1. The linear parts of anodic and cathodic Tafel regions appeared extended over wider current range in the case of $Fe_{59}Cr_{23}Mn_{12}Mo_6$. The calculated corrosion potential, E_{corr}, in the case of $Fe_{59}Cr_{23}Mn_{12}Mo_6$ is -431 mV with an associated corrosion current, I_{corr}, of 1.3×10^{-5} A/cm^2. The corresponding values of $Fe_{74}Cr_{24}Mo_2$ are -473 mV and 6.1×10^{-3} A/cm^2, respectively. The comparison of the values E_{corr} and I_{corr} indicated that addition of Mn and reduction of Fe resulted in the shift of the corrosion potential to a more negative value and appreciable decrease in the corrosion current density - two orders of magnitudes. Measured values are comparable to widely used in medicine 316L stainless steel in case of $Fe_{74}Cr_{24}Mo_2$ while values of $Fe_{59}Cr_{23}Mn_{12}Mo_6$ are considerably improved.

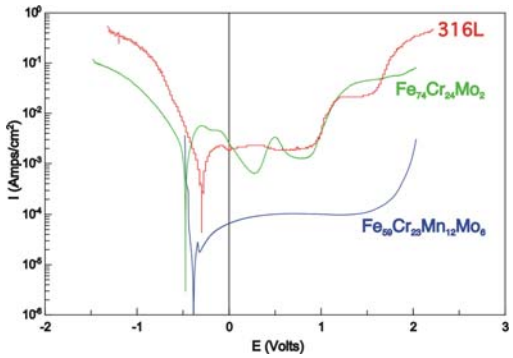

Fig. 4. The potentiodynamic curves of stainless steels in 0.1 M H_2SO_4 at 25 ^oC.

The potentiodynamic curve was characterized by the appearance of a well-defined anodic peak that appeared at -350 mV, which corresponds to an anodic peak current of 6.2×10^{-4} A/cm^2 for $Fe_{59}Cr_{23}Mn_{12}Mo_6$. On the other hand, the corresponding values for $Fe_{74}Cr_{24}Mo_2$ are -280mV and 5.3×10^{-2}A/cm^2, respectively.

Table 1. Results of corrosion tests.

Chemical composition	Icorr [A/cm^2]	Ecorr [mV]	Rp [Ohm/cm^2]	Corrosion rate [MPY]
$Fe_{74}Cr_{24}Mo_2$	$6.1*10^{-3}$	-473	$2.2*10^{1}$	$4.7*10^{1}$
$Fe_{59}Cr_{23}Mn_{12}Mo_6$	$1.3*10^{-5}$	-431	$1.5*10^{3}$	$7.4*10^{0}$
316L	$3.6*10^{-3}$	-349	$4.5*10^{2}$	$3.3*10^{1}$

The polarization resistance values, R_p, calculated from the potentiodynamic curve were 1.467×10^3 and 2.2×10^1 Ohm/cm^2 for $Fe_{59}Cr_{23}Mn_{12}Mo_6$ and $Fe_{74}Cr_{24}Mo_2$, respectively. The corresponding calculated corrosion rates are 7.4 and 4.7×10^1 MPY (milli-inch per year), respectively, that resulted in lowering of ca. 85% in the rate of corrosion of the stainless steel in the 0.1 M H_2SO_4 solution.

3.2. Ti-ceramic nanocomposites

X-ray diffraction was also employed to study the effect of mechanical alloying on Ti-HA composites. The typical XRD patterns of titanium and hydroxyapatite before

mechanical alloying are shown in Fig. 5 a, b. During MA process the original sharp diffraction lines of the sintering powders gradually become broader and their intensity decreases with milling time (Fig. 5c). The peak broadening represents a reduction in the crystallite size and increase in the internal strain in the mechanically alloyed materials. After 44 h of MA, the amorphous phase forms directly from the starting mixture, without formation of other phases (Fig. 5d).

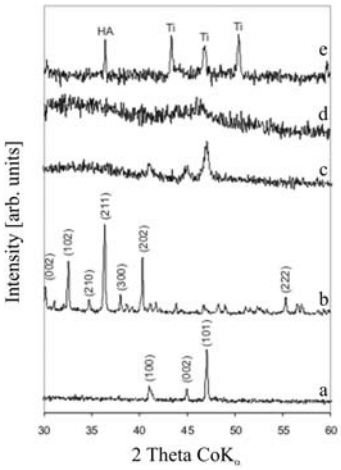

Fig. 5. XRD spectra of Ti and HA (10 vol%) powders mechanically alloyed for different times: (a) Ti - 0 h, (b) HA - 0 h, (c) 10 h, (d) 44 h, (e) after annealing at 1150 °C for 2 h.

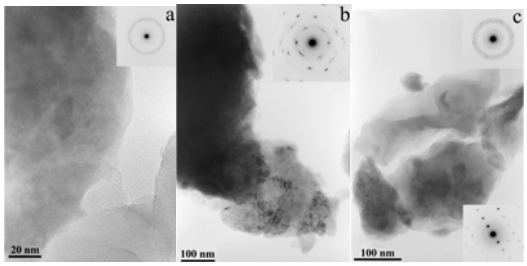

Fig. 6. TEM micrographs and electron diffraction patterns (insets) of the milled Ti-10 vol% HA sample for 44 h: (a) typical amorphous fragment, (b) same fine-crystalline phase, (c) crystalline grain.

The microstructure of milled titanium and hydroxyapatite powder was also studied by TEM. The sample milled for 44 h was mostly amorphous (broad rings in the SEAD pattern) as appears from high resolution image (Fig. 6a). Apart from prevailing amorphous phase, there is small amount of fine-crystalline (Fig. 6b) and crystalline phases (Fig. 6c). Lack of any sharp reflections in the XRD pattern suggests that the amount of the crystalline phase is very low and/or it forms during in TEM observation. During TEM studies, it has been found that the amorphous powders was unstable upon exposure to electron beam and underwent some crystallization.

During MA process of Ti-silica (10 wt%), the intensity of diffraction line of titanium decreases and after 20 h of milling has transformed completely to an amorphous phase, without formation of any other phases. TEM results shows that the powder milled for 20 h was mostly amorphous.

Formation of the bulk nanocomposites were achieved by annealing of the amorphous materials in high purity gas atmosphere composed of 95% Ar and 5% H_2 at 1150 ºC for 2 h (Fig. 5e). XRD analysis of Ti-10 vol% SiO_2 showed the presence of α-Ti type structure with cell parameters a = 2.972 Å, c = 4.774 Å. The formation of crystalline SiO_2 phase was not observed. In the XRD patters from the Ti-10 vol% HA composite after thermal treatment, there is present α-Ti (with cell parameters a = 2.774 Å, c = 4.494 Å) and apatite peaks. In this diagram, there is a shift of the titanium peaks towards larger angles. According to the Scherrer method of XRD profiles, the average size of heat treated Ti-HA and Ti-SiO_2 nanocomposites is about 30-40 and 40-50 nm, respectively.

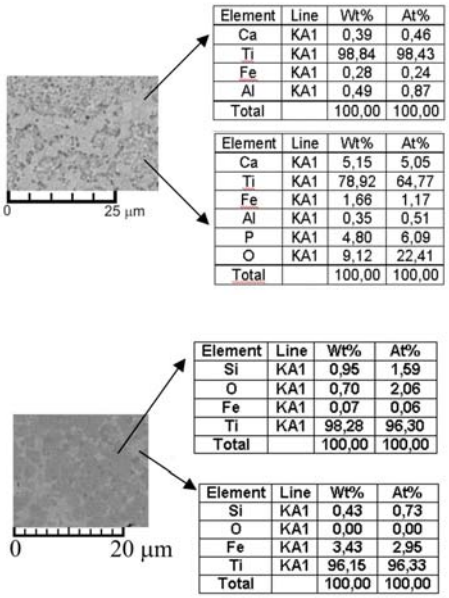

Element	Line	Wt%	At%
Ca	KA1	0,39	0,46
Ti	KA1	98,84	98,43
Fe	KA1	0,28	0,24
Al	KA1	0,49	0,87
Total		100,00	100,00

Element	Line	Wt%	At%
Ca	KA1	5,15	5,05
Ti	KA1	78,92	64,77
Fe	KA1	1,66	1,17
Al	KA1	0,35	0,51
P	KA1	4,80	6,09
O	KA1	9,12	22,41
Total		100,00	100,00

Element	Line	Wt%	At%
Si	KA1	0,95	1,59
O	KA1	0,70	2,06
Fe	KA1	0,07	0,06
Ti	KA1	98,28	96,30
Total		100,00	100,00

Element	Line	Wt%	At%
Si	KA1	0,43	0,73
O	KA1	0,00	0,00
Fe	KA1	3,43	2,95
Ti	KA1	96,15	96,33
Total		100,00	100,00

Fig. 7. EDS spectra of surface of: (top) Ti-10 vol% HA, (bottom) Ti-10 vol% SiO_2 nanocomposites mechanically alloyed for 44h and heat treated at 1150 ˚C for 2h.

The results of EDS analysis and scanning electron micrograph of the surface of sintered Ti-HA and Ti-SiO_2 nanocomposites mechanically are shown in Fig. 7. The phase constitution of Ti-10 vol% HA nanocomposite consists of titanium matrix with calcium and titanium matrix with apatite, which Ca/P ratio was 1.07, a value similar to the Ca/P ratio in $Ca_2P_2O_7$ (Fig. 7a). The presence of secondary HA phases are the result of cooling from a high temperature. Besides, the existence of Ti can degrade the structural stability of HA crystal and promote its decomposition [16]. The existence of second phase of HA in the composites can influence the final properties of sintered Ti-HA nanocomposites.

EDS results indicate that the predominant phase in Ti-SiO_2 composites is titanium with content of silica or

silicon particles. The presence of some amount of iron atoms in the sintered nanocomposites, could be explained by Fe impurities trapped in the MA powders from erosion of the milling media [17].

Change of processing parameters, like mechanical alloying and annealing times, as well as the chemical compositions and microstructure of titanium-ceramic nanocomposites leads also to a distribution of the properties [18]. The Vickers' microhardness of the sintered nanocomposites exhibit various distribution corresponding to constitutional change and increased with the rise of ceramic contents. The Vickers' hardness strongly increases for Ti-10 vol% HA nanocomposites (1500 $HV_{0,2}$) and is six times higher than of pure microcrystalline Ti metal (250 $HV_{0,2}$); see Fig. 8.

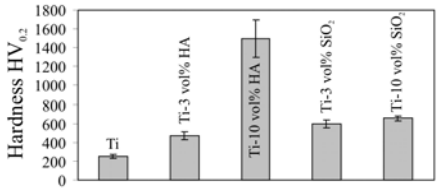

Fig. 8. Hardness of studied Ti-based nanocomposites

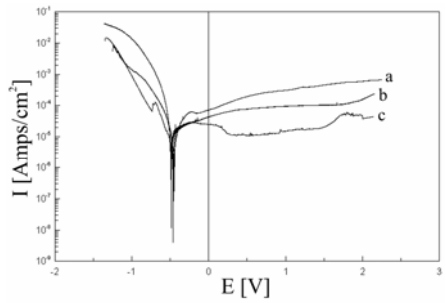

Fig. 9. Potentiodynamic polarization curves of: (a) Ti-10 vol% SiO_2, (b) Ti-10 vol% HA and (c) Ti in the 1M H_2SO_4 distilled water solution.

The polarization data obtained for sintered composites and microcrystalline titanium, including corrosion potentials (E_C), corrosion current densities (I_C) and corrosion rate (C_R) values are summarized in Table 2. Titanium composites with silica have better corrosion resistance than that with hydroxyapatite. From Table 2 it is possible to observe low values of corrosion rate, especially for Ti-10 vol% SiO_2 nanocomposite. Titanium composite with 10 vol% of HA or SiO_2 ceramic were more corrosion resistance ($I_c = 1.1\times10^{-6}$ Amp/cm^2, E_c= -0.48 V; $I_c = 9.23\times10^{-7}$ Amp/cm^2, E_c= -0.45 V, respectively) than microcrystalline titanium ($I_c = 1.49\times10^{-5}$ Amp/cm^2, E_c= -0.47 V); Fig. 9.

Future application of Ti-ceramic composites focuses our attention on the biological properties of Ti-HA and Ti-SiO_2 composite. Therefore, the biocompability of Ti-ceramic nanocomposites is currently investigated experimentally in our laboratory. It is expected that the studies may supply useful indirect information about the influence of the HA or SiO_2 on the osteointegration ability of fabricated nanocomposites.

Table 2. Mean values of corrosion current densities, corrosion potentials and corrosion rate of studied Ti-HA and Ti-SiO_2 nanocomposites

sample	I_C [Amp/cm^2]	E_C [V]	C_R [mm/y]
Ti-10 vol % HA	$1.1 \cdot 10^{-6}$	-0.48	0,03
Ti-10 vol% SiO_2	$9.23 \cdot 10^{-7}$	-0.45	0,02
Ti (microcrystalline)	$1.49 \cdot 10^{-5}$	-0.47	0,42

4. Conclusion

In this work, the structure, mechanical and corrosion properties of nanocrystalline nickel-free austenitic stainless steels and Ti-ceramic nanocomposites synthesized by mechanical alloying and powder metallurgical process were studied. Different phase constitution has significant influence on the mechanical and corrosion properties of sintered materials. The Ti-HA and Ti-SiO_2 nanocomposites mainly consist of different apatite or silica and silicon particles, respectively, reinforced with titanium matrix. Ti-10 vol% HA or SiO_2 nanocomposites possesses better mechanical and corrosion properties than microcrystalline titanium.

Acknowledgements

The financial support of the Polish Ministry of Education and Science under the contract No N507 071 32/2092 is gratefully acknowledged.

References

[1] J. S. Benjamin, Sc. American **234**, 40 (1976).
[2] C. Suryanarayna, Progr. Mater. Sc. **46**, 1 (2001).
[3] H. N. Liu, T. J. Webster, Biomaterials **28**, 354 (2007).
[4] S. K. Sahoo, S. Parveen, J. J. Panda, Nanomedicine: Nanotechnology, Biology and Medicine **3**, 20 (2007).
[5] J. K. Vasir, M. K. Reddy, V. D. Labhasetwar, Curr. Nanosci. **1**, 47 (2006).
[6] K. Niespodziana, K. Jurczyk, M. Jurczyk, J. Alloys Comp. (2007), in print.
[7] K. Jurczyk, K. Niespodziana, M. Jurczyk, Europ. J. Med. Res. **11**, 133 (2006).
[8] A. Yamamoto, Y. Kohyama, D. Kuroda, T. Hanawa, Mat. Sc. Eng. C **24**, 737 (2004).
[9] X. Liu, P. K. Chu, Ch. Ding, Mater Sci Eng. **47**, 49 (2004).
[10] F. Takeshita, Y. Ayukawa, S. Iyama, K, Murai, T. Suetsugu, J. Biomed. Mater. Res. **37**, 235 (1997).
[11] M. Long, H. J. Rack: Biomaterials **19**, 1621 (1998).
[12] M. A. Khan, R. L. Williams, D. F. Williams, Biomaterials **20**, 765 (1999).
[16] C. Chu, P. Lin, Y. Dong, X. Xue, J. Zhu, Z. Yin, J. Mater. Sci. Mater. Med. **13**, 985 (2002).
[17] M. Jurczyk, K. Smardz, W. Rajewski, L. Smardz, Mater Sci Eng, A **303**, 70 (2001).
[18] K. Niespodziana, K. Jurczyk, M. Jurczyk, Nanopages **1**, 219 (2006).

*Corresponding author: jurczyk@sol.put.poznan.pl